ARL-TR-10320 ● APR 2026

Next-Generation Cobalt-Free Tungsten Carbide Enabled by FeNiZr Binder Alloys

by Sean J. Fudger, Kenneth Brown, Billy C. Hornbuckle, Thomas L. Luckenbaugh, Philip E. Goins, and Kristopher A. Darling

NOTICES

Disclaimers

The findings in this report are not to be construed as an official Department of the Army position unless so designated by other authorized documents.

Citation of manufacturer's or trade names does not constitute an official endorsement or approval of the use thereof.

Destroy this report when it is no longer needed. Do not return it to the originator.

ARL-TR-10320 ● APR 2026

Next-Generation Cobalt-Free Tungsten Carbide Enabled by FeNiZr Binder Alloys

Sean J. Fudger, Billy C. Hornbuckle, Thomas L. Luckenbaugh, Philip E. Goins, and Kristopher A. Darling
DEVCOM Army Research Laboratory

Kenneth Brown
Global Tungsten & Powders Corp.

REPORT DOCUMENTATION PAGE

1. REPORT DATE	2. REPORT TYPE	3. DATES COVERED	
		START DATE	END DATE
April 2026	Technical Report	1/1/2020	3/12/2026

4. TITLE AND SUBTITLE
Next-Generation Cobalt-Free Tungsten Carbide Enabled by FeNiZr Binder Alloys

5a. CONTRACT NUMBER	5b. GRANT NUMBER	5c. PROGRAM ELEMENT NUMBER
5d. PROJECT NUMBER	**5e. TASK NUMBER**	**5f. WORK UNIT NUMBER**

6. AUTHOR(S)
Sean J. Fudger, Kenneth Brown, Billy C. Hornbuckle, Thomas L. Luckenbaugh, Philip E. Goins, and Kristopher A. Darling

7. PERFORMING ORGANIZATION NAME(S) AND ADDRESS(ES)	8. PERFORMING ORGANIZATION REPORT NUMBER
DEVCOM Army Research Laboratory ATTN: FCDD-RLA-MF Aberdeen Proving Ground, MD 21005	ARL-TR-10320

9. SPONSORING/MONITORING AGENCY NAME(S) AND ADDRESS(ES)	10. SPONSOR/MONITOR'S ACRONYM(S)	11. SPONSOR/MONITOR'S REPORT NUMBER(S)

12. DISTRIBUTION/AVAILABILITY STATEMENT
DISTRIBUTION STATEMENT A. Approved for public release: distribution unlimited.

13. SUPPLEMENTARY NOTES

14. ABSTRACT
Cemented tungsten carbide (WC) is widely used in cutting, machining, mining, and defense applications due to the exceptional hardness and high modulus provided by the WC phase combined with the plasticity and toughness imparted by the cobalt (Co) binder. Despite its widespread use, Co has been identified as both a strategic and critical material by the U.S. Department of the Interior and as a substance anticipated to be a human carcinogen by the U.S. Department of Health and Human Services, motivating the development of alternative binder systems that maintain the performance of conventional WC–Co materials. In this work, nanostructured FeNiZr is evaluated as a potential Co replacement due to its favorable mechanical properties and reduced health and supply-chain concerns. WC–FeNiZr composites were fabricated using both commercial press-and-sinter processing and field-assisted sintering followed by hot isostatic pressing, producing near–fully dense materials with hardness values exceeding 13.5–16.0 GPa (1377–1630 HV) and fracture toughness values up to 15 $MPa \cdot m^{1/2}$ (10 $ksi \cdot inch^{1/2}$). Microstructural characterization using scanning electron microscopy, electron backscatter diffraction, and transmission electron microscopy were used to investigate the structure–property relationships governing these materials. In addition, tribological wear testing was conducted to compare the performance of WC–FeNiZr composites with conventional WC–Co systems, while machine learning approaches were employed to guide materials development by enabling efficient exploration of complex, multifactorial processing–composition–property relationships.

15. SUBJECT TERMS
Sciences of Extreme Materials, tungsten carbide, WC, cobalt, Co, binder, FeNiZr

16. SECURITY CLASSIFICATION OF:			17. LIMITATION OF ABSTRACT	18. NUMBER OF PAGES
a. REPORT	b. ABSTRACT	C. THIS PAGE		
UNCLASSIFIED	UNCLASSIFIED	UNCLASSIFIED	UU	34

19a. NAME OF RESPONSIBLE PERSON	19b. PHONE NUMBER *(Include area code)*
Sean J. Fudger	(520) 691-4836

STANDARD FORM 298 (REV. 5/2020)
Prescribed by ANSI Std. Z39.18

Contents

List of Figures

List of Tables

1. Introduction*

More than a century ago, tungsten carbide (WC) was combined with cobalt (Co) to create a new class of materials exhibiting an exceptional combination of strength, toughness, and hardness. Initially developed for wire drawing dies, liquid phase–sintered WC–Co composites rapidly found broader application in machining, mining, ammunition, and other wear-intensive environments due to their outstanding mechanical performance. Despite the extensive industrial use of WC–Co systems for nearly a century, recent attention has focused on the potential health and supply-chain concerns associated with the Co binder phase. Evaluations by the U.S. Department of Health and Human Services and the International Agency for Research on Cancer concluded that Co compounds are possibly carcinogenic to humans based on studies involving inhalation exposure in test animals.[1] Furthermore, Co has been identified as a strategic and critical material by the U.S. Department of the Interior because a large portion of global Co production originates from Central Africa, where political instability can significantly influence supply availability and cost.[2]

The extremely high melting point of pure WC (~2800 °C) presents challenges for direct manufacturing and consolidation.[3] As a result, WC is typically processed as a composite material in which WC particles are combined with a metallic binder phase in powder form and consolidated through liquid phase sintering (LPS) at substantially lower temperatures (~1450 °C for WC–Co systems). In this structure, the hard WC grains provide exceptional hardness and stiffness, while the metallic binder phase contributes ductility and toughness. Typical WC–Co materials containing approximately 10 wt% Co and WC grain sizes near 1 μm exhibit densities around 14.5 g/cm, transverse rupture strengths approaching 3 GPa, hardness values near 15 GPa (~1530 HV), and fracture toughness values around 10–11 MPa $m^{1/2}$.[4–6] Because of this balanced property combination, cemented carbides remain essential materials for cutting tools, machining inserts, mining equipment, and numerous structural wear applications.

In response to the health and supply concerns associated with Co, considerable research has been directed toward identifying alternative binder materials capable of maintaining or improving the performance of conventional WC–Co systems. Numerous candidate binders have been investigated. For example, Schubert et al.[7] explored iron (Fe)-based binder systems; Fernandes et al.[8] investigated nickel (Ni)-based Co alternatives; Li et al.[9] examined the effects of chromium (Cr) and titanium

* GenAI (Gemini Enterprise edition) was utilized to blend some paragraphs, removing redundant information while maintaining overall flow. The authors re-read and reviewed all content and have verified the technical content is accurate.

(Ti) additions to Co binders; and Silva et al.[10] investigated copper (Cu)-based binder systems for WC composites. While the objective of these studies is often to enhance mechanical performance or tailor materials for specific applications, any viable binder candidate must first satisfy several fundamental industrial requirements. These include good wettability with WC particles, a sufficiently low melting temperature to enable practical commercial processing, and adequate solubility for tungsten and carbon to avoid the formation of undesirable phases during cooling.

Murdoch and Darling[11] further expanded these criteria by highlighting the importance of liquid binder viscosity and capillary behavior within the WC–binder system, both of which strongly influence densification and microstructure evolution during sintering. Based on these considerations, several multicomponent alloy systems were evaluated and compared with the performance of Co in conventional cemented carbides. Among these, Fe–Ni–Zr (iron–nickel–zirconium) alloys were identified as promising binder candidates because they satisfy many of the thermodynamic and processing criteria required for effective WC consolidation. Within the WC–FeNiZr phase diagram, the binder exhibits a compositional carbon range in which stoichiometric carbon balance can be maintained through small additions of free carbon, thereby avoiding the formation of eta phases (M_6C) or graphite during sintering.[12] In addition, the formation of small quantities of ZrC has been shown experimentally to inhibit WC grain growth, contributing to improved microstructural stability during consolidation.[12]

Cemented carbides are typically fabricated through LPS, where the molten binder provides a pathway for rapid densification and subsequently solidifies to form a tough metallic matrix surrounding the WC grains. However, the incorporation of novel multicomponent binders such as FeNiZr introduces additional complexities that must be carefully controlled during processing. These include potential issues related to incomplete densification, formation of deleterious phases, and heterogeneous binder distribution if consolidation parameters are not optimized.[13] Consequently, recent research has explored alternative consolidation methods capable of improving densification and microstructural control in WC composites containing advanced binder systems.

One promising approach involves the use of field-assisted consolidation techniques such as direct current sintering (DCS) (a.k.a., spark plasma sintering), often combined with hot isostatic pressing (HIP). These techniques offer several advantages over conventional furnace-based LPS. Rapid heating and cooling cycles significantly reduce processing times, improving manufacturing efficiency and throughput. Direct electrical heating of the powder compact also improves energy efficiency compared with traditional furnace heating. Additionally, the ability to

sinter at lower temperatures reduces the risk of undesirable chemical reactions and microstructural degradation while enabling improved control of grain growth and phase formation.[14]

DCS fundamentally combines the simultaneous application of thermal, mechanical, and electrical energy through the use of applied pressure, temperature, and pulsed direct current. Because the powder's compact and tooling materials are electrically conductive, relatively low voltages (typically <10 V) generate extremely high electrical currents (5–30 kA) passing through the powder bed. This produces rapid internal joule heating, enabling heating rates approaching 1000 °C min^{-1} and facilitating near-complete densification in short processing times.[15] Following consolidation, HIP can be used to further eliminate residual porosity through diffusion bonding, creep deformation, and plastic flow under high-temperature and high-pressure conditions.

In addition to mechanical performance considerations, tribological behavior is a critical factor in determining the suitability of alternative binder systems for cemented carbide applications. Sliding wear occurs in many environments where lubrication is limited, including cutting tools, bearings, mechanical seals, and forming dies. Wear resistance in cemented carbides is strongly influenced by microstructure, particularly WC grain size, binder composition, hardness, and operating conditions.[16] As the majority of existing tribological studies focus primarily on WC–Co materials, comparatively little information exists regarding the wear performance of cemented carbides containing alternative multicomponent binders. Consequently, systematic evaluation of tribological performance is necessary to determine the viability of new binder systems.

Recent advances in computational tools have also enabled the incorporation of machine learning (ML) approaches into materials development workflows. In particular, active-learning frameworks based on Gaussian Process Regression (GPR) models can be used to guide experimental design by identifying promising regions of composition–processing space while simultaneously quantifying prediction uncertainty.[17–20] These methods are particularly well-suited to materials science applications where experimental datasets are often sparse, and complex relationships exist among processing parameters and resulting material properties. By iteratively selecting experiments that reduce model uncertainty or maximize target properties, such as hardness or wear resistance, active-learning strategies can significantly accelerate materials discovery and optimization. Implementation of these approaches using Python-based environments and ML libraries such as Scikit-Learn and ModAL provide a flexible framework for integrating experimental data with predictive modeling.[21–25]

Taken together, these developments highlight the growing potential of nanostructured FeNiZr binder systems as alternatives to conventional Co binders in cemented WC composites. The present work therefore investigates the feasibility of consolidating WC–FeNiZr materials using advanced and industrially relevant processing techniques while examining the resulting microstructure, mechanical properties, and tribological performance. Through the integration of experimental characterization and data-driven analysis, this research aims to assess the potential of FeNiZr binders for next-generation Co-free cemented carbide systems.

2. Materials and Methods

2.1 Powder Preparation

The studies evaluated WC–FeNiZr powder blends prepared using nanocrystalline FeNiZr binders synthesized in-house by high-energy mechanical alloying. In the DCS-/HIP-based studies, a powder blend of 90 wt% WC and 10 wt% Fe–Ni–Zr was used, with the WC powder obtained from Global Tungsten & Powders (GTP) (Towanda, Pennsylvania) and having an average particle size of 0.67 μm.[14] Two binder chemistries were investigated in those studies: Fe_{88}-Ni_8-Zr_4 and Fe_{91}-Ni_8-Zr_1 (at%), which are hereafter denoted as Fe-Ni-Zr_4 and Fe-Ni-Zr_1, respectively. In the press-and-sinter (P&S) study, the FeNiZr binder consisted of Fe-Ni-Zr_1 (at%) and was blended with a midsize WC grade produced by GTP having an average particle size of 3.8 μm; both 10 wt% and 12 wt% FeNiZr binder contents were evaluated.[13]

For binder synthesis, raw Fe, Ni, and Zr powders (−325 mesh; 99.9%, 99.9%, and 99.5% pure, respectively; American Elements, American Elements, and Materion) were loaded into a Zoz CM08 rotary ball mill (Zoz GmbH, Germany) using a 10:1 ball-to-powder mass ratio with 6.35-mm (1/4-inch) stainless steel balls.[26] Milling was carried out for 30 h at subzero temperature to limit cold welding, yielding a homogeneous, unagglomerated powder with individual particle sizes between 5 and 50 μm.[26,27] The as-milled FeNiZr grain size was approximately 15 nm, as determined by the Scherrer method.[27,28] These nanocrystalline FeNiZr powders belong to a class of oxide-dispersion strengthened (ODS) ferritic alloys, which are known for high-temperature mechanical stability and radiation resistance.[29–31] In these systems, a ferritic Fe-/Ni-based matrix contains a dispersion of nanoscale oxide particles that can contribute to strengthening and thermal stability.

Following binder production, the WC and FeNiZr powders were blended using low-energy milling conditions chosen to smear and distribute the binder phase without causing significant further WC grain refinement.[12] In the DCS-/HIP-based routes, an 8:1 ball-to-powder mass ratio of 4.76-mm (3/16-inch) WC balls was used

for blending. Two carbon-addition strategies were examined for the WC–FeNiZr mixtures. In the first, carbon was introduced by pickup from the Nalgene milling bottle, following an energy/time recipe reported by Pittari et al.[12] In the second, stearic acid was added directly to the powder prior to mixing at 240 rpm for 12 h.[21] Both methods yielded relatively homogeneous binder distributions surrounding the WC particles.

In the P&S route, the ready-to-press mixture was produced using a lab-scale attritor mill charged with 6.35-mm WC–Co balls, midsize WC powder (GTP grade S45), FeNiZr binder powder, and 2 wt% paraffin wax, with heptane as the milling medium.[13] Milling was conducted for 2 h at 150 rpm in an Ironman attritor mill manufactured by Grove Gear. Following mixing, the excess heptane was decanted, the powder was separated from the media using a no. 10 sieve, the remaining heptane was removed using a Buchi R215 Rotovapor with F100 chiller, and final drying was conducted on a steam table in a Fisher fume hood.[13]

2.2 Consolidation

Two primary consolidation routes were employed across the studies: 1) DCS followed by HIP and 2) conventional P&S processing.

For the DCS/HIP studies, the blended powders were loaded into a 40-mm (1.57-inch) cylindrical carbon–carbon composite die lined with GRAFOIL and boron nitride high-temperature release spray.[14,21] Prior to sintering, the powders were pre-compacted with a 4500-kg (10,000-lb) load to ensure proper die-punch placement. Sintering was then performed in an FCT HP D 125 DCS furnace (FCT Systeme GmbH, Germany). The DCS cycle began with a 20-kN (4500-lb) preload and chamber evacuation, followed by preheating from room temperature to 450 °C, the lower measurement limit of the optical pyrometer. The powder compact was subsequently heated from 450 °C to the target temperature over 8 min, with processing temperatures ranging from 1100 to 1300 °C and dwell times of 15–30 min investigated. At the maximum temperature, the compacts were consolidated under an applied pressure of 100 MPa (14.5 ksi). After the dwell period, the pressure was released and the samples were allowed to cool under vacuum within the chamber.[14,21]

Following DCS, the resulting pucks were postprocessed by instrumented HIP (American Isostatic Presses; Columbus, Ohio) to improve densification. A high-temperature eddy current sensor was used to monitor densification as a function of temperature. The samples were heated from room temperature to 1300 °C at 10 °C/min under high-purity Ar at 207 MPa (30 ksi) for 60 min.[14,21]

In the P&S study, transverse rupture strength specimens were pressed in a Carver 3980.4NE00 01 press to 12 tsi (~165 MPa) using a 1.25-inch (31.8-mm) × 0.50-inch (12.7-mm) compaction die.[13] Additional application parts were produced using a 0.3185-inch (8.09-mm) × 0.9186-inch (23.3-mm) die. The compacted samples were then placed on a graphite plate and sintered using the cycle shown in Figure 1.

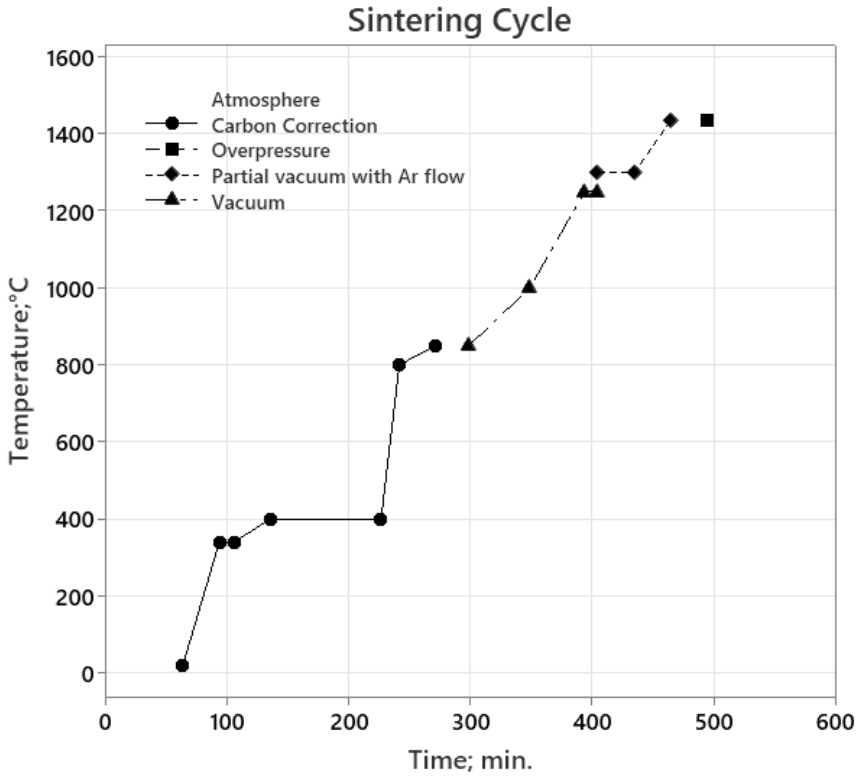

Figure 1. Sintering cycle applied to WC–FeNiZr consolidation.[13]

2.3 Characterization

2.3.1 Density, Hardness, and Toughness

In all three studies, density was measured using the Archimedes technique. For the DCS/HIP materials, the theoretical density (TD) of the raw powder was 14.46 g/cm^3 based on the elemental constituent ratios.[14,21] For the P&S materials, the TD ranged from 13.94 to 14.31 g/cm^3 depending on binder content and carbon addition.[13]

Specimens were prepared following standard ceramographic procedures for hardness, toughness, and microscopy. In the DCS/HIP studies, samples were prepared following ISO 28079 for Palmqvist toughness testing and subsequent microscopic analysis.[32,33] Hardness was evaluated using an array of ten 2-kg Knoop

indentations on polished cross sections. In accordance with ASTM C1326, the Knoop hardness HK, in GPa, was calculated using Equation 1[32]:

$$HK = 0.014229\frac{P}{d^2} \quad (1)$$

where P is the indentation load (N) and d is the long diagonal length of the indentation (mm).

Palmqvist indentation toughness was measured from three 50-kgf (491 N) Vickers indentations following ISO 28079.[33] Crack lengths were measured from the four corners of each indentation and inserted into Equation 2 to calculate the Palmqvist toughness W_K[33]:

$$W_K = A\sqrt{HV}\sqrt{\frac{F}{T}} \quad (2)$$

where A is a fitting constant ($A = 0.0028$), HV is the hardness in N/mm^2, F is the indentation load (N), and T is the sum of the crack lengths (mm).[33]

2.3.2 Microstructural Characterization

Microstructural analysis in all three studies was performed using a Nova NanoSEM 600 scanning electron microscope (FEI; Hillsboro, Oregon) operating at 20 keV in both secondary- and backscattered-electron modes.[13,14,21] Scanning electron microscopy (SEM) was used to assess porosity, grain size, binder morphology, and consolidation characteristics, and in the P&S materials specifically to examine the possible presence of eta phase and graphite.[13]

Electron backscatter diffraction (EBSD) was used to characterize grain morphology and binder behavior. Samples were prepared for EBSD using a Leica EM TIC 3X ion milling system to obtain high-quality polished cross sections with improved contrast. EBSD analysis incorporated EDAX spherical harmonic-based indexing together with neighbor pattern averaging and reindexing in OIM analysis, using a bandwidth of 63, grid size of 128, and a scan step size of 0.04 μm.[13] EBSD maps were generated using a 5-pixel minimum grain size, 0.05 confidence index minimum filter, and a scan step size of 0.1 μm.[14]

Additional characterization was performed in the DCS/HIP studies. Transmission electron microscopy (TEM) was used to evaluate the binder grains and local diffraction behavior. TEM was performed on a JEOL 2100F operated at 200 kV, with TEM foils prepared by lift-out and thinning in a ThermoFisher Scientific Helios G4 dual-beam microscope, followed by final thinning at 5 kV to minimize beam damage.[14]

2.3.3 Chemical Analysis

Select chemical analysis is included to better establish processing–microstructure–property relationships, especially as it relates to eta/graphite formation due to stoichiometric imbalances. Energy-dispersive spectroscopy (EDS) was used to characterize localized elemental variations.[14] In addition, bulk chemical analysis was performed using combustion infrared detection (ASTM E1019-18[34]), inert gas fusion (ASTM E1019-18 and E1447-22[35]), and direct current plasma emission spectroscopy (ASTM E1097-12[36]) for the quantification of carbon/sulfur, oxygen/nitrogen, hydrogen, and metallic elements, respectively.

2.4 Wear Testing

Because WC–FeNiZr materials are being considered for wear applications, initial tribological testing was incorporated to assess their suitability under conditions relevant to cutting and machining tools.[21] Conventional ASTM methods for cemented carbide wear evaluation often rely on abrasion tests such as ASTM B611 or ASTM G65.[37,38] However, to better support high-throughput materials screening, a high-rate rotary ball-on-disc tribometer approach based on ASTM G99-23 was selected.[39] This method more closely mimics the unidirectional sliding and contact stresses experienced by a machine-tool insert.[38]

The counterface material selected in the initial study was 52100 steel, a high-carbon chromium alloy steel. The WC–FeNiZr materials were used as the disc specimens in all configurations, with other ball/disc combinations reserved for future work.

Wear-Test Sample Preparation

For wear testing, WC discs were consolidated by the tandem DCS + HIP route described above.[14] The nominal as-consolidated disc size was 40-mm diameter × 10-mm thickness. These were subsequently electrical discharge machined into 25.4-mm (1.0-inch) diameter × 5-mm (0.1963-inch) thickness specimens to avoid the previously observed core–rim structure. The discs were then polished to an arithmetic average surface roughness of less than 0.8 μm and machined to fit the Bruker CETR-UMT rotary stage (Figure 2). Ball and pin materials were cleaned by sonication in acetone for 10 min, followed by ethanol for 10 min, to remove surface contaminants.[21]

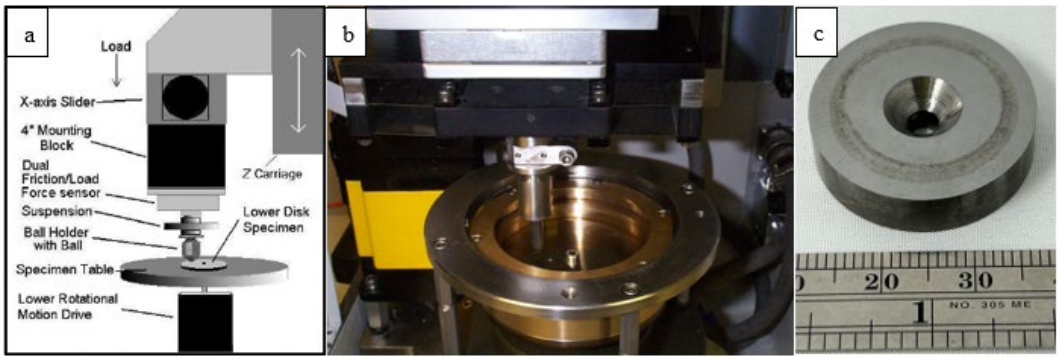

Figure 2. a) Schematic and b) image of Bruker CETR-UMT multi-specimen test system with ball/pin-on-disk system setup with rotational stage[38] and c) example disc geometry with visible wear track.

3. Results and Discussion

This collective research shows WC–FeNiZr can be consolidated to high density using either tandem DCS + HIP or commercial P&S routes; however, the resulting hardness, toughness, and microstructure depend strongly on binder chemistry, carbon control, binder fraction, WC grain size, and consolidation temperature. Across the full dataset, two broad property trends emerge. First, the $FeNiZr_4$ compositions consolidated by DCS tend to exhibit higher hardness but lower toughness than WC–Co benchmarks. Second, the $FeNiZr_1$ compositions and the 12 wt% FeNiZr P&S compositions show marked toughness gains, but with a corresponding reduction in hardness. This indicates that the FeNiZr system offers a tunable hardness–toughness balance rather than a single direct replacement for WC–Co.

3.1 Consolidation Response and Mechanical Properties

As shown by Table 1, the DCS consolidation temperature had only a modest effect on densification of the nano WC 10% ($FeNiZr_4$) material over 1100–1300 °C, with post-HIP densities remaining near 95% TD. In contrast, hardness varied substantially. The 1200 and 1250 °C conditions produced the highest hardness values, 16.7 ± 0.8 GPa and 16.5 ± 1.0 GPa, respectively; whereas, the 1300 °C condition exhibited a sharp drop to 9.0 ± 2.1 GPa. This drop was paired with a slight increase in toughness, suggesting the onset of binder liquefaction or excessive softening, rather than a predominantly solid-state consolidation response behavior under the combined influence of temperature, pressure, and current.

Table 1. Consolidation conditions and resulting properties of WC–FeNiZr materials compared with standard commercial WC–Co materials.[13,14,21]

Sample description	Temp. (°C)	Hold (min)	Density (g/cm^3)	%TD post-DCS	%TD post-HIP/final %TD	HK2 (GPa)	Wk (MPa·m$^{1/2}$)	Wk (ksi·in$^{1/2}$)
Nano WC-10% ($FeNiZr_4$) (Nalgene)	1100	15	13.77	94.5	95.2	15.0 ± 1.3	8.5 ± 0.2	7.7 ± 0.2
Nano WC-10% ($FeNiZr_4$) (Nalgene)	1200	15	13.95	95.5	95.5	16.7 ± 0.8	8.7 ± 0.3	7.9 ± 0.3
Nano WC-10% ($FeNiZr_4$) (Nalgene)	1250	15	13.88	95.2	95.3	16.5 ± 1.0	8.1 ± 0.4	7.4 ± 0.4
Nano WC-10% ($FeNiZr_4$) (Nalgene)	1300	15	13.94	94.9	95.2	9.0 ± 2.1	9.1 ± 0.6	8.3 ± 0.5
Nano WC-10% Co	1450	. . .	14.43	. . .	98.5	15.5 ± 0.1	10.2 ± 0.0	9.3 ± 0.0
Micro WC-10% Co	1450	. . .	14.43	. . .	98.5	14.7 ± 0.2	10.5 ± 0.2	9.6 ± 0.2
Nano WC-10% ($FeNiZr_1$) (Stearic)	1250	30	14.18	95.7	98.1± 0.7	10.0 ± 2.5	13.5 ± 1.5	12.3± 1.4
P&S midsize WC-12% $FeNiZr_1$ (0.10% C added)	1480	. . .	13.94	. . .	100	13.1 ± 0.3	15.1 ± 0.8	13.7± 0.7
P&S midsize WC-10% $FeNiZr_1$ (0.05% C added)	1480	. . .	14.21	. . .	100	13.8 ± 0.2	9.8 ± 0.1	8.9 ± 0.1
P&S midsize WC-10% $FeNiZr_1$ (0.10% C added)	1480	. . .	14.18	. . .	100	13.5 ± 0.4	10.2 ± 0.4	9.3 ± 0.4

Compared with the commercially produced nano and micro WC–10% Co controls, the $FeNiZr_4$ DCS materials processed below 1300 °C exceeded or matched WC–Co hardness but remained inferior in toughness. This trade-off motivated the development of the $FeNiZr_1$ variant, which was expected to provide improved formability because prior work on the standalone binder showed lower elevated-temperature strength and greater room-temperature ductility/plasticity than $FeNiZr_4$.[28–30] In practice, the nano WC–10% ($FeNiZr_1$) material consolidated at 1250 °C and post-HIP to 98.1% TD produced a much higher toughness of 13.5 ± 1.5 MPa·m$^{1/2}$, surpassing both WC–Co controls, but at a substantially lower hardness of 10.0 ± 2.5 GPa. Thus, within the DCS/HIP route, $FeNiZr_1$ shifts the balance toward toughness, whereas $FeNiZr_4$ shifts it toward hardness.[14,21]

The commercial P&S results in Table 1 reinforce the same conclusion but from an industrial processing perspective. All three WC–$FeNiZr_1$ compositions reached 100% TD, demonstrating that the binder system is compatible with full

densification under conventional processing. The 12 wt% $FeNiZr_1$ + 0.10% C composition exhibited the highest toughness of the entire combined dataset, 15.1 ± 0.8 $MPa \cdot m^{1/2}$, while maintaining a hardness of 13.1 ± 0.3 GPa. Increasing binder content from 10 wt% to 12 wt% therefore raised toughness by roughly 50% while reducing hardness by only about 5%, making binder fraction a particularly effective design variable in the P&S route. By contrast, the 10 wt% FeNiZr + 0.05% C condition yielded higher hardness (13.8 ± 0.2 GPa) but lower toughness (9.8 ± 0.1 $MPa \cdot m^{1/2}$), consistent with carbon deficiency and eta-phase formation.[13]

The mechanical-property results show that WC–FeNiZr does not behave as a single compositionally fixed replacement system. Instead, the binder architecture can be tuned for two distinct property envelopes: 1) high hardness, moderate density, and limited toughness in DCS/HIP $FeNiZr_4$ materials; and 2) high toughness with moderate hardness in $FeNiZr_1$ or higher–binder-fraction P&S materials.

3.2 SEM Observations: Porosity, Binder Pooling, and Phase Segregation

The SEM results reveal clear differences in how the FeNiZr binders redistribute during consolidation. In the P&S materials, Figure 3 shows that the WC–Co control exhibited the most uniform binder distribution, although disseminated pores roughly 5 μm in diameter remained, consistent with the measured 98.5% TD. By contrast, each WC–FeNiZr P&S composition displayed scattered binder pools, some reaching about 10 μm along the long axis, and these pools became more frequent when the binder content was increased to 12 wt%. The WC–10$FeNiZr_1$ 0.05 C sample additionally showed dark-gray regions identified as eta phase (Fe_3W_3C), confirming the strong sensitivity of this system to carbon balance. In that condition, the eta phase was associated with a harder but more brittle material response, in agreement with the property data in Table 1.

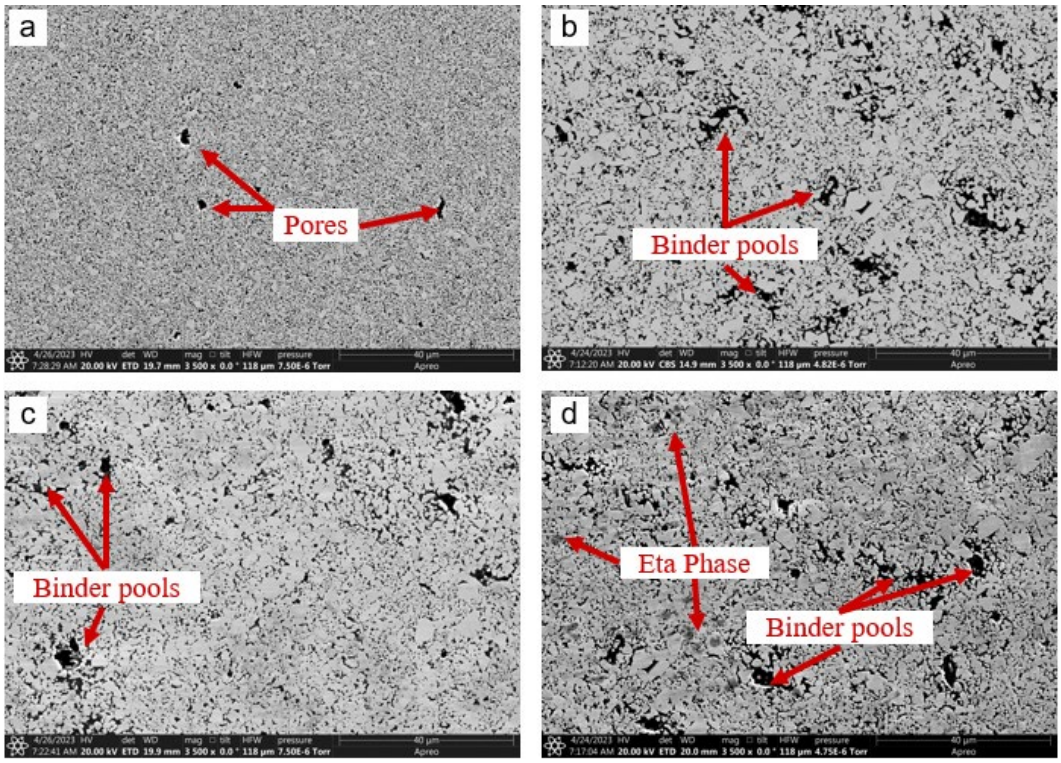

Figure 3. SEM images of a) WC–Co, b) WC–12FeNiZr 0.10 C, c) WC–10FeNiZr 0.10 C, and d) WC–10FeNiZr 0.05 C.[13]

The DCS/HIP $FeNiZr_4$ series showed an even stronger dependence of binder–pool morphology on processing conditions. As illustrated in Figure 4, the 1100 and 1200 °C conditions produced especially large and frequent binder pools, with long-axis dimensions approaching approximately 80 µm.[14] At higher magnification, the 1250 °C condition displayed distinct grayscale regions within the binder pools, indicating phase separation. EDS point analysis from these regions, summarized in Table 2, showed WC-like chemistry at spot 2, Zr-rich regions at spots 3 and 7 consistent with possible ZrC, and Cr-rich regions at spots 4 and 6 suggestive of Cr-containing carbides or more complex oxide/carbide phases. Spot 5 most closely represented the typical ternary FeNiZr binder.[14] The presence of trace V and Cr was notable because neither was intentionally added during blending; the likely sources were WC raw-powder additives such as Cr_3C_2 or process contamination from tooling and media.[40]

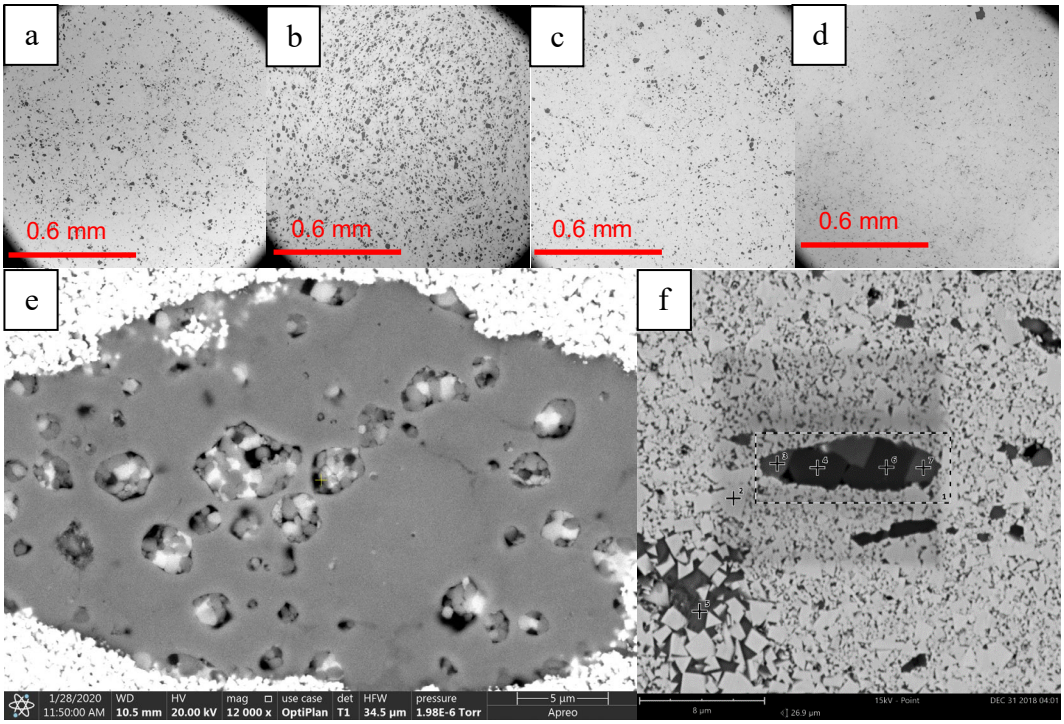

Figure 4. Backscattered electron images of WC–FeNiZr$_4$ consolidated at a) 1100 °C (2012 °F), b) 1200 °C (2292 °F), c) 1250 °C (2282 °F), d) 1300 °C (2372 °F), e) 1250 °C (2282 °F) condition under 12kX magnification, and f) 1250 °C (2282 °F) condition under 15kX magnification with EDS points highlighted corresponding to Table 2.[14]

Table 2. EDS quantification of select areas within WC–FeNiZr$_4$ binder pools.[14]

Location	C (at%)	O (at%)	V (at%)	Cr (at%)	Fe (at%)	Ni (at%)	Zr (at%)	W (at%)
2	74.33	2.63	. . .	. . .	. . .	. . .	. . .	23.04
3	74.6	11.63	. . .	. . .	0.36	. . .	10.91	2.5
4	51.5	25.91	. . .	12.63	6.94	. . .	0.19	2.83
5	47.57	. . .	. . .	. . .	42.65	3.46	0.11	6.21
6	49.65	27.33	0.69	12.62	7.15	. . .	0.16	2.41
7	74.28	12.27	. . .	. . .	0.22	. . .	11.74	1.49

Compared with FeNiZr$_4$, the FeNiZr$_1$ DCS/HIP material displayed a much finer binder morphology, with no binder pools larger than about 15 µm and no obvious second-phase regions in the SEM observations reported. This difference aligns with the higher final density and greater toughness of the FeNiZr$_1$ materials and suggests that lowering Zr content reduces coarse phase separation while improving formability during post-DCS HIP densification.[14,21]

3.3 EBSD Observations: WC Grain Morphology, Eta Phase, and Zirconia-Bearing Phases

The EBSD results from all three studies consistently show that the WC–FeNiZr microstructures differ from WC–Co not only in binder morphology but also in WC grain shape and phase composition. In the P&S materials, Figure 5 shows that the WC–Co control had a finer and more angular WC grain morphology than the FeNiZr materials.[13] The FeNiZr-containing samples exhibited blunted and rounded WC grains, which the authors attributed to changes in the WC dissolution/reprecipitation process, potentially caused by lower W solubility in the FeNiZr binder and by interference from ZrO_2 precipitates and eta-phase islands.[13] The WC–10FeNiZr$_1$ 0.05 C condition was especially revealing. Figure 6 shows the confirmed presence of Fe_3W_3C eta phase concentrated within binder regions and along WC–binder interfaces. The EBSD phase map also indicated measurable amounts of monoclinic ZrO_2, with minor tetragonal and cubic contributions.[13]

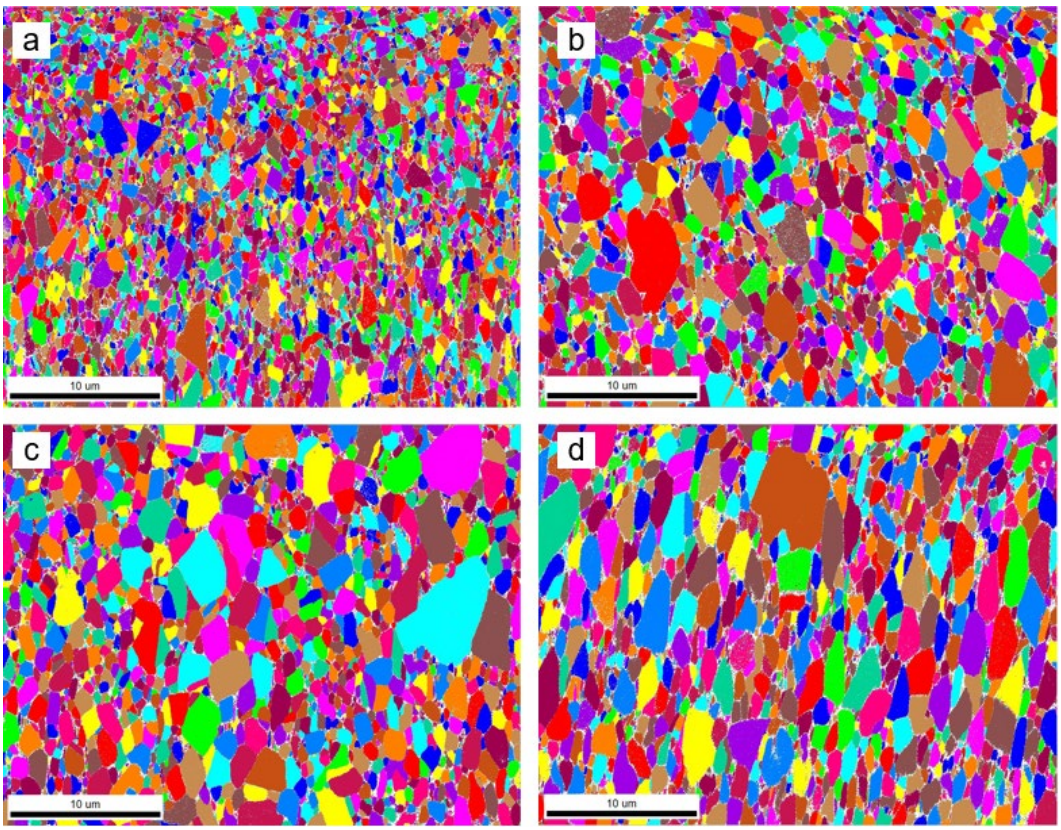

Figure 5. EBSD unique grain color maps of a) WC–Co, b) WC–12FeNiZr$_1$ 0.10 C, c) WC–10FeNiZr$_1$ 0.10 C, and d) WC–10FeNiZr$_1$ 0.05 C.[13]

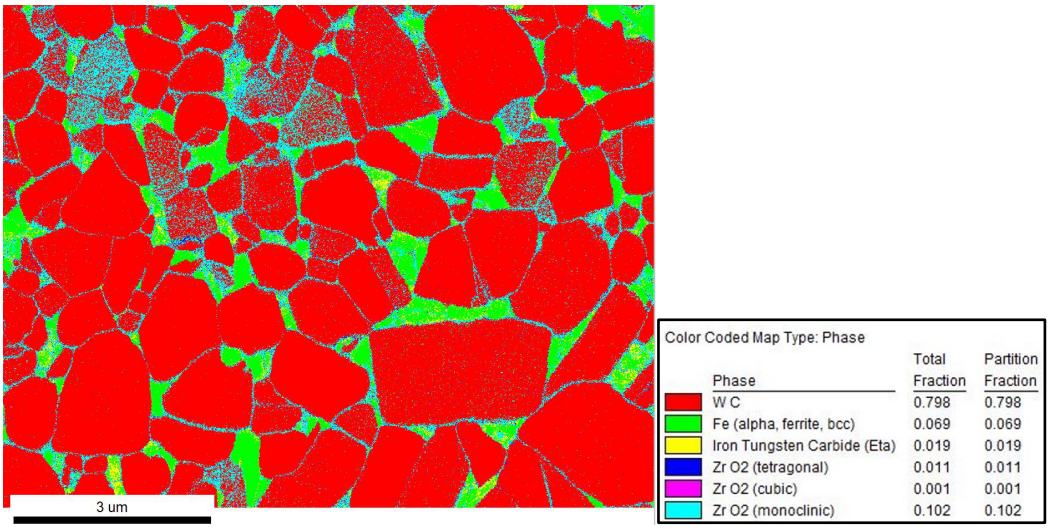

Figure 6. EBSD generated phase map for sintered WC–10FeNiZr$_1$ 0.05 C.[13]

The DCS/HIP studies reproduced the same broad morphology trends. In Figure 7, the micro WC–10% Co material again exhibited well-indexed, sharp-cornered WC grains, while both the FeNiZr$_1$ and FeNiZr$_4$ materials showed blunted or nearly rounded grain corners. Additionally, a discontinuous network of binder pools is observed in the WC–FeNiZr materials, the largest around 15 µm, along with some Ni-rich local regions consistent with the binder composition. Although the FeNiZr$_4$ phase map was shown, no large regions of concentrated Zr were resolved, likely because the Zr is dispersed as a very fine oxide distribution throughout the binder and along grain boundaries.[21]

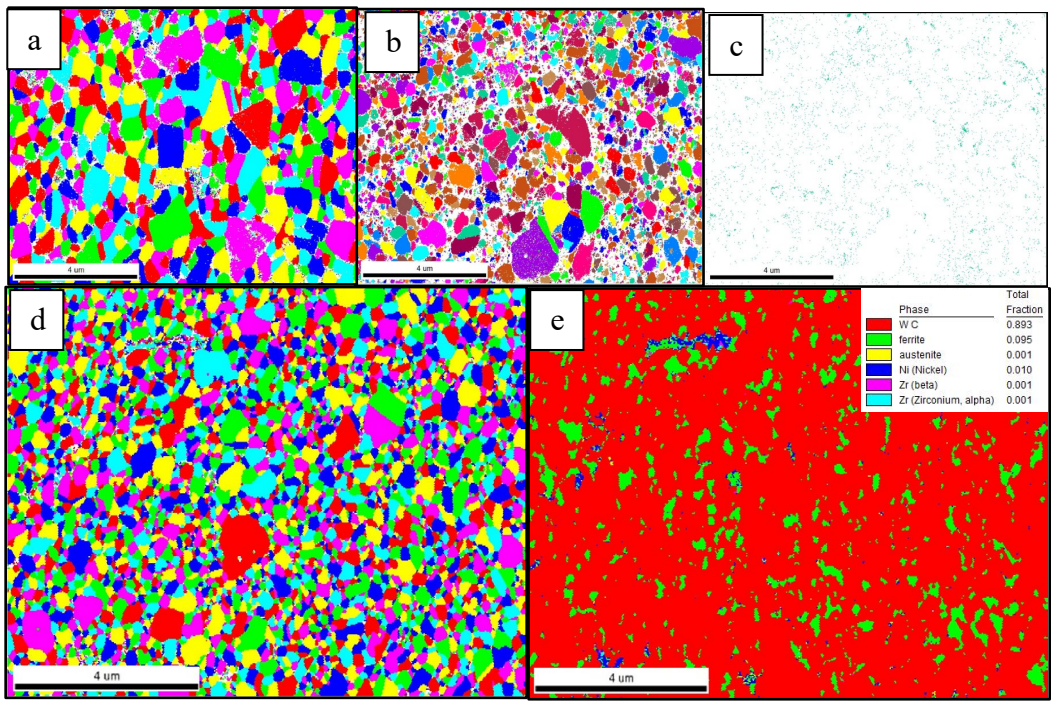

Figure 7. EBSD unique grain color maps of a) micro WC–10% Co, b) nano WC–10% ($FeNiZr_1$), c) EBSD phase map of WC–10% ($FeNiZr_1$) with eta phase (W_3Fe_3C) shown in green, d) nano WC–10% ($FeNiZr_4$), and e) nano WC–10% ($FeNiZr_4$) phase map inset with area fraction of each phase.[14,21]

Also evident in Figure 7 is $FeNiZr_1$ material containing appreciable tungsten–iron carbide (W_3Fe_3C) in the EBSD phase map, concentrated in the binder and interfacial regions. This is important because the $FeNiZr_1$ material was mechanically superior in toughness, yet still chemically carbon deficient in the measured bulk composition. Thus, the improved toughness of $FeNiZr_1$ cannot be attributed to the absence of eta phase; instead, it likely reflects a competing benefit from the greater formability and ductility of the lower-Zr binder during densification. In other words, the $FeNiZr_1$ system appears to tolerate some eta-phase formation while still delivering a net toughness advantage due to improved binder response.[14,21]

3.4 Bulk Chemistry and Stoichiometric Constraints

The bulk chemical analysis reported in Table 3 provides strong support for the conclusion that carbon control is one of the primary limiting variables in WC–FeNiZr processing. The composition for the nano WC–10% ($FeNiZr_1$) material: W 83.4 wt%, C 5.34 wt%, Fe 9.1 wt%, Ni 0.81 wt%, Zr 0.21 wt%, and O 1.05 wt%, along with trace Co, Ti, Cr, and very low V.

Table 3. Bulk chemical analysis of nano WC–10% ($FeNiZr_1$) sample performed via combustion infrared detection, inert gas fusion, and direct current plasma emission spectroscopy.

Element	wt%
Tungsten	83.4
Carbon	5.34
Iron	9.1
Nickel	0.81
Zirconium	0.21
Oxygen	1.05
Cobalt	0.014
Titanium	0.002
Chromium	0.02
Vanadium	<0.0005

The weight percentages of the binder constituents are in line with the expected $FeNiZr_1$ material. Co was measured at 0.014 wt% in the bulk. In addition to the aforementioned source, another possible origin of Co contamination could be from the milling process: WC–Co balls are used as milling media and the Zoz mill spindle has a Stellite (Co–Cr alloy) coating. Consistent with the identification of chromium via EDS, bulk analysis shows 0.02 wt% is present in the nano WC–10% ($FeNiZr_1$) sample. Again, two possible sources being Cr_3C_2 as an additive to the tungsten or contamination from the Stellite. The measured carbon level of 5.34 wt% lies below the narrow acceptable range of roughly 5.72 wt% to 5.76 wt% needed to avoid both eta-phase and graphite formation in this system.[12]

This is entirely consistent with the EBSD and SEM observations showing eta phase in the carbon-deficient conditions. It is common for oxides to be present on the surface of all powders used in making cemented WC. Although care was taken during the storage and processing of these powders (utilizing an Ar atmosphere glovebox), the introduction of oxygen is unavoidable during the powder transfer to consolidation equipment. The measured oxygen content is 1.05 wt%. Further reducing the oxides would decrease final porosity in the sintered compact.[14,21]

The combined chemistry and phase data therefore support a central result of all three studies: WC–FeNiZr is considerably less forgiving than WC–Co with respect to carbon stoichiometry, and small deviations in carbon content can strongly alter the balance between hardness and toughness through eta-phase formation.

3.5 TEM Evidence from the $FeNiZr_1$ Binder

Figure 8 shows a TEM foil, lifted out from a region containing both WC and binder, revealing distinct second-phase particles within the binder and a microstructure dominated by lath martensite, together with a visible prior-austenite grain boundary intersecting one of the second-phase particles. The martensite is usually associated

with much faster cooling rates than those used after DCS; however, the 8 at% Ni level is sufficient to reduce the critical cooling rate and permit martensitic transformation.[14] The observed lath morphology was also consistent with the carbon introduced during processing; higher carbon levels would be expected to produce a more lenticular morphology. These observations suggest that the $FeNiZr_1$ binder is not a simple equilibrium ferritic matrix after processing, but rather a rapidly transformed, multiphase metallic binder whose transformation behavior may play an important role in toughness development.

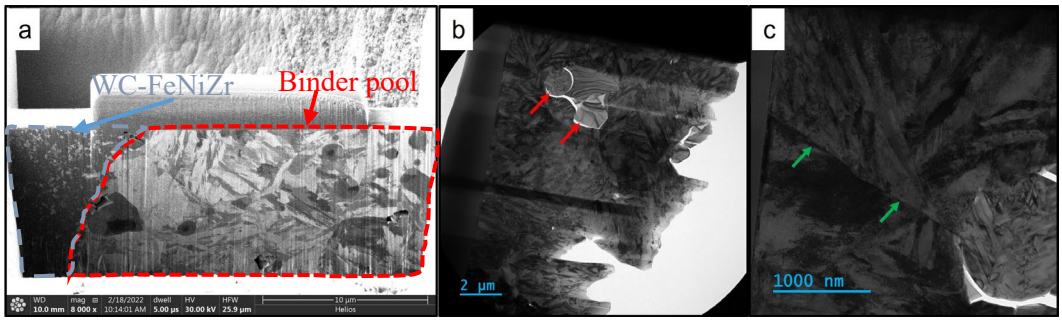

Figure 8. a) SEM image of a focused ion beam lift-out of a nano WC–10% ($FeNiZr_1$) sample highlighting the selected region containing both WC particles and a $FeNiZr_1$ binder pool. b) Corresponding low magnification TEM bright field image illustrating the underlying structure of the binder with second phase particles present. c) Corresponding high magnification TEM bright field image highlighting the presence of martensite and a pre-austenite grain boundary.[14]

3.6 Mechanistic Interpretation of the Hardness–Toughness Trade-off

Mechanical alloying produces nanoscale ZrO_2 containing clusters or coherent oxide dispersions in the FeNiZr binders, and these dispersions contribute to strengthening together with nanocrystalline grain refinement through the Hall–Petch effect.[27,30,31] The high number density of these particles also improves thermal stability in the standalone ODS binders, which is particularly important because the binder is generally the weakest link in the composite, especially in high-stress and high-temperature applications.[13,14,21]

At the same time, these strengthening advantages are strongly modified by the higher processing temperatures used in sintering and HIP. The DCS/HIP studies explicitly suggest that grain growth and oxide-particle coarsening continue at the elevated temperatures used for consolidation, progressively reducing binder strength. This helps explain why the $FeNiZr_4$ materials retain high hardness at 1200–1250 °C but soften dramatically by 1300 °C; and why $FeNiZr_1$, though more formable and more easily densified, becomes much softer after thermal exposure.

In short, $FeNiZr_4$ appears thermally more stable but less ductile, whereas $FeNiZr_1$ is more ductile and densifiable but more prone to softening through coarsening.[14,21]

WC grain size further modifies this balance. There is an obvious difference between nano and micro starting WC powders in the EBSD maps, and the finer WC–Co microstructure was one reason for its relatively high hardness. The results indicate that smaller WC grain size improves hardness, making grain-size control a second major design variable in addition to binder chemistry and carbon content.[12,14,21]

3.7 Wear-Testing Feasibility and ML Guidance

Although full tribological comparison against WC–Co was not yet completed, it along with WC–FeNiZr materials optimized for wear applications—namely, binder volume fraction, binder alloy composition, and carbide additions to name a few—will be completed at a future date. High-rate and high-throughput testing utilizing a ball-on-disc wear platform could operate at up to 5000 rpm and 1000 N, conditions that approach the loading rates experienced in machining.[21] A minimum of three wear tracks could be produced on each specimen face, indicating that the setup is appropriate for high-throughput screening of composition, load, cutting speed, and counter-face effects. Figure 9 shows cutting force and flank wear width as a function of machining time and removed volume for a baseline WC–Co material; it was presented to anchor the relevance of the selected wear regime.

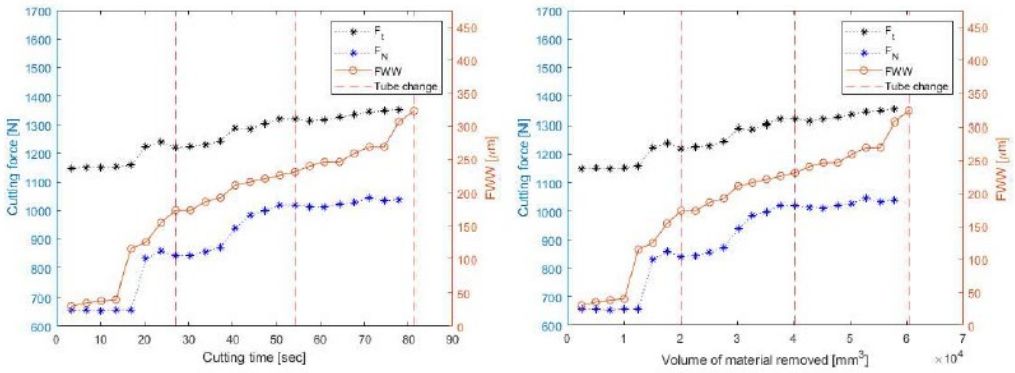

Figure 9. Cutting force and flank wear width as a function of time and material removed during machining of baseline WC–Co material.[21]

This work also introduces a preliminary active-learning/GPR framework for navigating the complex WC–FeNiZr experimental space. Using a small dataset that combines hardness measurements, the model achieved an average $R^2 \approx 0.83$ over repeated train-test splits and predicted a modest reduction in hardness with increasing consolidation temperature for Co, $FeNiZr_4$, and $FeNiZr_1$ systems.[21] While the authors correctly noted that the dataset was still too sparse for statistically robust optimization, the model already identified informative next experiments and

demonstrated how uncertainty-guided experimentation could accelerate exploration of this high-dimensional processing–composition space. The broader implication is that the FeNiZr system is sufficiently multifactorial that ML–assisted experiment planning is likely to be especially valuable as future wear and multi-property datasets expand.[21]

An example of a property–relationship prediction is shown in Figure 10. The model generally agrees with the experimentally observed trends discussed in this work. However, the limited size of the dataset results in large uncertainty within the GPR model. Consequently, the predictions are not yet statistically significant beyond the model's confidence interval, limiting the ability of the initial model to draw firm conclusions regarding the success of these preliminary efforts or to identify an optimal experimental combination.[21]

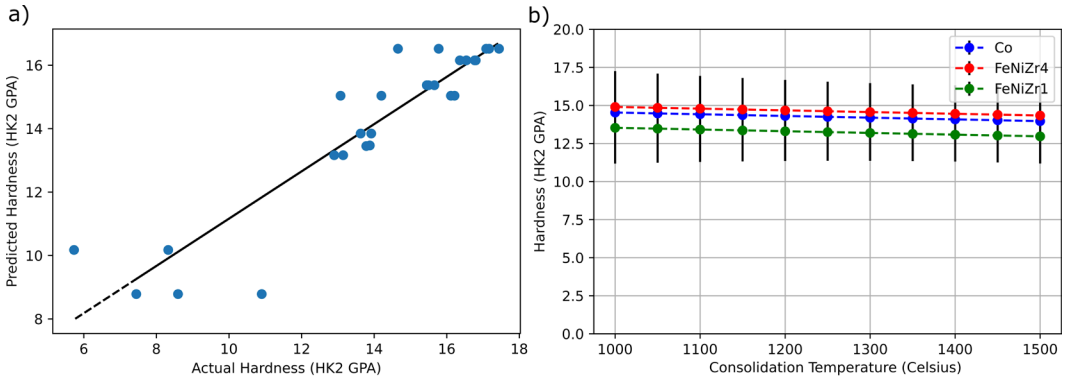

Figure 10. a) Representative test-train split (median-performant split) with predicated and actual hardness values for given compositions and processing parameters. b) Model predictions of consolidation temperature vs. hardness.[21]

Predictions of hardness as a function of temperature were generated for binder compositions containing Co, $FeNiZr_4$, and $FeNiZr_1$. In all cases, the model predicts a modest decrease in hardness with increasing temperature. Although the associated uncertainty remains relatively large, reflecting both model uncertainty and experimental variability in the measured hardness values, the overall trends predicted by the model are consistent with the expected behavior of the system based on physical understanding.[21]

However, the active-learning component of the model identifies the next experimental conditions that will most effectively increase the learning rate of the system and reduce uncertainty as rapidly as possible as the program progresses, providing significant value during the early stages of development. In these initial stages, the learning agent selects candidate experiments based on the predicted uncertainty within the pool of possible samples. The sample space boundaries are defined and discretized, and each point within the eight-dimensional parameter space is evaluated at each experimental step. As additional data are collected, this

uncertainty-driven learning strategy will be replaced by a more advanced learner designed for multi-objective, multi-fidelity optimization. In this framework, more readily measured properties such as hardness can be used to accelerate learning more difficult-to-measure responses, including wear resistance, using an approach like those recently reported in the literature.[21]

4. Conclusions

The following conclusions can be drawn from this work:

1) FeNiZr-based binders ($FeNiZr_1$ and $FeNiZr_4$) were successfully integrated with WC using both conventional P&S processing and tandem DCS followed by HIP. These results demonstrate the feasibility of FeNiZr alloys as environmentally friendly Co-free binders for cemented carbide systems.
2) Mechanical properties of WC–FeNiZr composites exhibit tunable hardness–toughness behavior relative to WC–Co. WC–$FeNiZr_1$ compositions achieved fracture toughness values exceeding WC–Co, with WC–12$FeNiZr_1$–0.10 C demonstrating an over 40% improvement in toughness (15.1 vs. 10.5 $MPa \cdot m^{-1/2}$). In contrast, WC–$FeNiZr_4$ compositions achieved hardness values exceeding those of WC–Co.
3) Microstructural analysis identified multiple second-phase constituents within the binder, including Cr- and Zr-containing particles. TEM observations revealed a martensitic lath structure within the FeNiZr binder and the presence of nanoscale second-phase particles intersecting pre-austenite grain boundaries, indicating complex binder phase evolution during consolidation.
4) Carbon balance and consolidation conditions strongly influence phase stability and densification. Continued optimization of binder chemistry and processing parameters will be necessary to achieve fully dense materials capable of simultaneously exceeding WC–Co in both hardness and toughness.
5) A ML–assisted active-learning framework demonstrates strong potential for accelerating binder optimization. Even with limited initial data, the GPR model achieved an average R^2 of approximately 0.83, while a high-rate pin-on-disc wear testing approach provided an effective platform for high-throughput evaluation and iterative model improvement.
6) Overall, the combined results support FeNiZr as a credible Co-replacement binder family, but not yet as a direct one-to-one substitution under all processing conditions. Instead, the data suggest that FeNiZr is best viewed as a property-tailorable binder platform whose successful deployment will depend on precise control of carbon stoichiometry, Zr level, binder fraction, WC grain size, and consolidation history.

5. References

1. U.S. Department of Health and Human Services. Health effects. Toxicological profile for cobalt. Public Health Service, National Toxicology Program; 2011. 2004 Apr edition. p. 11–54.
2. DLA. Strategic materials. Defense Logistics Agency (US); n.d. [accessed 2022 Jan]. www.dla.mil/HQ/Acquisition/Strategic-Materials
3. Chychko A, García J, Collado Ciprés V, Holmström E, Blomqvist A. HV-KIC property charts of cemented carbides: a comprehensive data collection. Int J Refract Met Hard Mater. 2022;103:105763. ISSN 0263-4368.
4. Haynes WM, editor. CRC handbook of chemistry and physics. 92nd ed. CRC Press; 2011. p. 4.96. ISBN 1-4398-5511-0.
5. Groover MP. Fundamentals of modern manufacturing: materials processes and synthesis. 4th ed. Wiley; 2010.
6. Swab JJ, Wright JC. Application of ASTM C1421 to WC-Co fracture toughness measurement. Int J Refract Met Hard Mater. 2016;58:8–13.
7. Schubert WD, Fugger M, Wittmann B, Useldinger R. Aspects of sintering of cemented carbides with Fe-based binders. Int J Refract Met Hard Mater. 2015;49:110–123.
8. Fernandes CM, Senos AMR, Vieira MT, Antunes JM. Mechanical characterization of composites prepared from WC powders coated with Ni rich binders. Int J Refract Met Hard Mater. 2008;26:491–498.
9. Li N, Zhang WB, Peng YB, Du Y. Effect of the cubic phase distribution on ultrafine WC-10Co-0.5Cr-xTa cemented carbide. J Am Ceram Soc. 2016;99:1047–1054.
10. Silva VL, Fernandes CM, Senos AMR. Copper wettability on tungsten carbide surfaces. Ceram Int. 2016;42:1191–1196.
11. Murdoch HA, Darling KA. Metric mapping: a color coded atlas for guiding rapid development of novel cermets and its application to “green” WC binder. Mater Des. 2018;150:64–74.
12. Pittari JJ et al. Sintering of tungsten carbide cermets with an iron-based ternary alloy binder: processing and thermodynamic considerations. Int J Refract Met Hard Mater. 2018;76:1–11.

13. Fudger S et al. Microstructure and properties of cemented tungsten carbide with nanocrystalline FeNiZr binder. Advances in Additive Manufacturing with Powder Metallurgy—2023: Proceedings of the 2023 Additive Manufacturing with Powder Metallurgy Conference; 2023 June 18–21. Sponsored by the Metal Powder Industries Federation.

14. Fudger SJ, Luckenbaugh TL, Hornbuckle BC, Darling KA. Mechanical properties of cemented tungsten carbide with nanocrystalline FeNiZr binder. Int J Refract Met Hard Mater. 2024;118.

15. Suarez M et al. Challenges and Opportunities for spark plasma sintering: a key technology for a new generation of materials. In: Ertug B, editor. Sintering applications. IntechOpen; 2013. p. 319–342. Ch. 13.

16. Van der Merwe R, Sacks N. Effect of TaC and TiC on the friction and dry sliding wear of WC–6 wt% Co cemented carbides against steel counterfaces. Int J Refract Metals Hard Mater. 2013;41:94–102.

17. Cohn D, Atlas L, Ladner R. Improving generalization with active learning. Mach Learn. 1994;15:201–221.

18. Settles B. Active learning literature survey. University of Wisconsin–Madison (US); 2009. Technical Report No.: 1648.

19. Rasmussen CE, Willians CKI. Gaussian processes for machine learning. MIT Press; 2006. ISBN 0-262-18253-X.

20. Song J, Wei P, Valdebenito M, Beer M. Active learning line sampling for rare event analysis. Mech Sys Sig Proc. 2021;147:107113.

21. Fudger SJ, Goins PE, Berkebile SP, Darling KA. Wear evaluation of cemented tungsten carbide with nanocrystalline FeNiZr binder. Advances in Powder Metallurgy & Particulate Materials—2024: Proceedings of the International Conference on Powder Metallurgy & Particulate Materials; 2024 June 16–19; Pittsburgh, PA. Metal Powder Industries Federation.

22. Pedregosa F et al. Scikit-Learn: machine learning in Python. J Mach Learn Res. 2011;12:2825–2830.

23. Danka T, Horvath P. modAL: a modular active learning framework for Python. arXiv. 2018. arXiv:1805.00979 [cs.LG]. https://doi.org/10.48550/arXiv.1805.00979

24. Jacobs R, Goins PE, Morgan D. Role of multi-fidelity data in sequential active learning materials discovery campaigns: case study of electronic bandgap. Mach Learn Sci Tech. 2023;4(4):045060.

25. Gopakumar AM, Balachandran PV, Xue D, Gubernatis J, Lookman T. Multi-objective optimization for materials discovery via adaptative design. Sci Rep. 2018;8:3738.

26. Fudger SJ, Luckenbaugh TL, Roberts AJ, Haines CD, Darling KA. Tying processing parameters to the microstructure and mechanical properties of nanostructured FeNiZr consolidated via the field assisted sintering technique. Metals. 2019;9:436.

27. Kotan H, Darling KA. Isothermal annealing of a thermally stabilized Fe-based ferritic alloy. J Mater Eng Perform. 2015;24:3271–3276.

28. Langford JI, Wlison AJC. Scherrer after sixty years: a survey and some new results in the determination of crystalline size. J Appl Crystallogr. 1978;11:102–113.

29. Darling KA et al. Structure and mechanical properties of Fe-Ni-Zr oxide-dispersion-strengthened (ODS) alloys. J Nucl Mater. 2015;467:205–213.

30. Barton DJ et al. Microstructure and dynamic strain aging behavior in oxide dispersion strengthened $_{91}$Fe-$_{8}$Ni-$_{1}$Zr (at%) alloy. Mater Sci Eng A. 2018;725:503–509.

31. Hu YJ et al. Nano-sized superlattice clusters created by oxygen ordering in mechanically alloyed Fe alloys. Sci Rep. 2015;5:11772.

32. C1326-13. Standard test method for Knoop indentation hardness of advanced ceramics. ASTM International; 2013.

33. ISO 28079:2009. Hardmetals–Palmqvist toughness test. International Organization for Standardization; 2009.

34. ASTM E1019-18. Standard test methods for determination of carbon, sulfur, nitrogen, and oxygen in steel, iron, nickel, and cobalt alloys by various combustion and inert gas fusion techniques. ASTM International; 2024.

35. ASTM E1447-22. Standard test method for determination of hydrogen in reactive metals and reactive metal alloys by inert gas fusion with detection by thermal conductivity or infrared spectrometry. ASTM International; 2022.

36. ASTM E1097-12R17. Standard guide for determination of various elements by direct current plasma atomic emission spectrometry. ASTM International; 2017.

37. ASTM B611-21. Standard test method for determining the high stress abrasion resistance of hard materials. ASTM International; 2022.

38. ASTM G65-16. Standard test method for measuring abrasion using the dry sand/rubber wheel apparatus. ASTM International; 2021.

39. ASTM G99-17. Standard test method for wear and friction testing with a pin-on-disk or ball-on-disk apparatus. ASTM International; 2023.

40. Wittmann B, Schubert WD, Lux B. WC grain growth and grain growth inhibition in nickel and iron binder hardmetals. Int J Refract Met Hard Mater. 2002;20:51–60.

List of Symbols, Abbreviations, and Acronyms

Ar	Argon
ARL	Army Research Laboratory
C	Carbon
Co	Cobalt
Cr	Chromium
Cu	Copper
DCS	Direct Current Sintering
DEVCOM	U.S. Army Combat Capabilities Development Command
EBSD	Electron Backscatter Diffraction
EDS	Energy-Dispersive Spectroscopy
Fe	Iron
GPR	Gaussian Process Regression
GTP	Global Tungsten & Powders
HIP	Hot Isostatic Pressing
LPS	Liquid Phase Sintering
M	Molybdenum
ML	Machine Learning
Ni	Nickel
ODS	Oxide-Dispersion Strengthened
P&S	Press-and-Sinter
SEM	Scanning Electron Microscopy
TD	Theoretical Density
TEM	Transmission Electron Microscopy
Ti	Titanium
WC	Tungsten Carbide
wt%	Weight-Percent
Zr	Zirconium

1 (PDF)	DEFENSE TECHNICAL INFORMATION CTR DTIC OCA
1 (PDF)	DEVCOM ARL FCDD RLB CB TECH LIB